Composites: Part A 211 (2026) 110159

Contents lists available at ScienceDirect

Composites Part A

journal homepage: www.elsevier.com/locate/compositesa

Fracture behaviour of selectively z-pinned composite joints

G. Loi, F. Aymerich *

Department of Mechanical, Chemical and Materials Engineering, University of Cagliari 09123 Cagliari, Italy

ARTICLE INFO

Keywords:
Z-pinning
Joints
Fracture
Finite element modelling

ABSTRACT

This study examines the mechanical performance and damage evolution of single-step composite joints reinforced with edge-localised steel z-pins. A combined approach of experimental testing and finite element simulations is employed to evaluate the role of the pins in controlling strength and fracture processes. Results show that z-pinning significantly enhances structural capacity and damage tolerance, increasing ultimate strength and failure strain by approximately 16 % and 25 %, respectively. Both pinned and unpinned joints exhibit a similar damage sequence, initiated by resin cracking near the adherend ends followed by interfacial debonding. However, although debonding begins at similar strain levels in both joint types, the pins markedly reduce crack propagation rates. Visual and microstructural analyses show that the z-pins remain intact during loading while undergoing extensive plastic shear deformation upon final adherend separation. The FE model successfully reproduces the load–strain response and the damage evolution. The simulations show that z-pins enhance joint strength and fracture resistance through a dual mechanism: an initial shielding effect acting before the crack reaches the pins, which reduces crack driving energy by altering the local stress field ahead of the crack tip, followed by a bridging action once the crack propagates beyond the pin row.

1. Introduction

Over the past few decades, laminated fibre-reinforced composites have seen increasing use in primary structural applications owing to their combination of high specific strength and stiffness, tailorable anisotropic behaviour, superior fatigue resistance, excellent chemical resistance and enhanced damping capacity. However, the overall performance and durability of composite structures are frequently governed by the integrity of their joints and connections [1,2]. While joints are essential for assembling complex components, they often constitute the regions of highest stress concentration, where damage is most likely to initiate and propagate, ultimately leading to structural failure. As a result, the analysis and design of joint configurations play a critical role in ensuring structural reliability under static and fatigue loading conditions.

Adhesive joining—including bonding, co-bonding, and co-curing methods—is a highly effective joining method for composites, as it ensures uniform stress distribution and smooth surface finishes while preserving material continuity and reducing overall weight compared to mechanical fastening [1–4]. However, significant shear and peel stress concentrations typically develop at the ends of the overlap region. Given the inherently low interlaminar strength of laminated composites, failure often initiates at these sites, propagating either as delamination between layers or debonding along the joint interface.

Several approaches have been proposed to enhance the interlaminar resistance of laminated composites [5–10]. The introduction of through-thickness reinforcement in the form of threads (stitching, tufting) or rigid rods (z-pinning), is particularly effective as it directly addresses the inherent out-of-plane weaknesses of the material [11–21].

Through-thickness reinforcements such as stitches or z-pins enhance delamination resistance by providing a mechanical bridging mechanism across the fracture plane [6,18,22]. As a crack tip advances, these elements exert closure tractions that restrain opening and sliding relative displacements between the crack faces. The bridging action effectively mitigates the stress intensity at the crack tip, reducing the crack-driving energy available for propagation and thereby promoting a transition from unstable to gradual, progressive fracture. As joints are among the most critical sites for debonding or delamination initiation, several studies have been carried out to enhance the mechanical performance of composite connections by exploiting the bridging mechanism of through-the-thickness reinforcements [23]. Compared with stitching or tufting, z-pins are more suitable for insertion into prepreg layers and enable more easy and selective application in specific regions [24]. For this reason, most research aimed at improving composite joint

* Corresponding author.
E-mail address: francesco.aymerich@unica.it (F. Aymerich).

https://doi.org/10.1016/j.compositesa.2026.110159
Received 13 May 2026; Received in revised form 23 July 2026; Accepted 1 August 2026
Available online 3 August 2026
1359-835X/

performance via through-thickness reinforcement has focused on z-pinning as a toughening strategy for co-cured or co-bonded connections [25]. Special effort has been dedicated to the analysis of lap joints, which are the most common joining configurations found in structural composite applications and provide a suitable benchmark for evaluating the effectiveness of such reinforcements [13,26–35].

In this context, a thorough experimental campaign was carried out by Mouritz and co-workers, exploring the effects of z-pin density, diameter, and material on the strength and damage tolerance of joints between composite adherends [13,26–28,32]. The improvement achievable in the strength of single-lap carbon/epoxy joints using 0.28 mm diameter carbon z-pins distributed with a regular pattern across a 30 mm overlap was investigated in [26,27]. Their findings indicate that both tensile strength and strain at failure are highly sensitive to pin density and diameter. A pin density of 0.5 % resulted in an 8 % increase in strength, while a density of 2 % yielded a 41 % improvement. However, at a pin density of 4 %, the enhancement decreased to 23 %, indicating that the benefits of z-pinning diminish at high pin contents. The failure in joints with 0.5 % pin density was characterised by stable debonding growth, with final separation occurring after the complete fracture of the bond line followed by the shear rupture of the carbon z-pins. The observed improvement can be attributed to the crack-bridging mechanism of the z-pins, which transferred the applied shear stress across the adherend interface, thereby delaying debond propagation and promoting a more progressive failure evolution. Conversely, in joints with 2 % and 4 % pin densities, the initial interfacial debonding was arrested by the bridging action of the pins, with ultimate failure occurring through adherend rupture along a pin row. This indicates that at high pinning densities, the reinforcing benefits of the pins are partially offset by the effect of defects generated during z-pin insertion, such as fibre breakage, resin-rich pockets, fibre waviness and distortion. These defects introduce localised stress concentrations that, at high pin content, shift the failure mode from the bond line to the weakened laminate adherend. For the joints reinforced with 2 % pin density, it was also observed that increasing the pin diameter from 0.28 mm to 0.51 mm induced a transition in the failure mechanism, with the debonding crack propagating along the entire bond line and final separation of the adherends occurring by a combination of pin pull-out and pin shear failure.

Clear evidence of the dependence of joint performance on z-pin density has also been reported in other studies. Strength improvements of 6 % and 38 % were, for example, reported in [33] for co-cured glass fibre single-lap joints after inserting glass fibre pins with densities of 0.5 % and 2 %, respectively; however, the z-pinning efficiency diminished to 13 % at a 4 % density, showing that the beneficial toughening effect of the pins was significantly compromised by the detrimental influence of damage induced during the pinning process. A similar trend, where joint strength increased with pin density only up to a certain value before diminishing at higher densities, was observed in [35] for carbon/epoxy single-lap joints reinforced with carbon z-pins.

Enhancements in the mechanical and damage tolerance properties of composite lap joints have also been reported using metallic z-pins. It is worth noting that, under Mode II loading conditions—which represent the dominant loading mode in lap joints—metallic z-pins were found to be more effective than carbon fibre pins [36,37]. Their higher ductility allows them to sustain bridging tractions over larger sliding displacements, unlike the premature shear fracture typically observed in brittle carbon pins. Significant increases in strength (20 %) and, particularly, elongation limits (250 %) were for example presented in [32] for single-step joints reinforced at the overlap with a 2 % volume content of steel pins. The observed failure process initiated with the growth of interfacial cracks at the ends of the bonded region; thereafter, the z-pins progressively bridged the advancing cracks, retarding their propagation and allowing the lap joint to sustain an increasing load up to a peak value. At this point, the entire interface failed, causing an abrupt loss in the joint load-carrying capacity. However, due to the good shear strength of steel pins and the relatively high pin content [38], the traction loads still transmitted by the steel pins provided a residual—although much reduced—load-bearing capacity. This capacity decreased gradually with increasing strain due to progressive plastic deformation and pull-out of the z-pins, until they were completely pulled-out, leading to the total separation of the adherends.

Experimental investigations into the behaviour of quasi-isotropic carbon/epoxy single-lap joints reinforced with 0.5 mm steel z-pins at 2 % areal density were reported in [30,31]. The results showed that z-pinning increased the static strength of the joint by approximately 15 %, and that further improvements (reaching almost 30 %) could be obtained by providing the pins with a jagged surface to enhance interfacial adhesion with the embedding resin, thereby increasing the force required for pin pull-out. Significant improvements in joint strength were also reported in [29] with the insertion of staple-like steel pins at the overlap of double-lap joints between carbon/epoxy adherends. When inserted at the joint edges, staple-like pins may provide a dual effect, whereby the two through-thickness legs establish the bridging mechanism at the interface, while the transverse connecting portion (bridge) provides an alternative load path between the adherends that helps to mitigate stress concentrations at the bond line.

A different approach to the through-thickness reinforcement of composite joints involves the use of metal sheets incorporating protruding pins, which are inserted between the prepreg adherends [39–41]. However, while this reinforcing method offers improved accuracy and enhanced pull-out resistance, it presents several significant limitations: it lacks flexibility for localised reinforcement, is difficult to integrate into complex geometries, and introduces a notable weight penalty.

While the vast majority of studies on pinned joints focus on comprehensive pinning, where through-thickness reinforcements are uniformly distributed across the entire overlap region, only limited work is available on the efficacy of z-pins inserted at specific positions within the joint.

For example, it was reported in [40] that reinforcing single-lap joints by incorporating metal inserts with pins concentrated near the edges led to strength enhancements superior to those achievable with pins evenly distributed across the joint area. Our previous work [34] on stepped-lap joints reinforced with three or four rows of metal z-pins distributed across the overlap region resulted in an increase of approximately 15 % in static strength. Notably, however, the same strength increase could be achieved by reinforcing the joints with only two rows of pins placed near the overlap ends, thus suggesting that the major contribution to improving the load-carrying capacity of the joint is provided by the z-pins next to the edges. These preliminary results demonstrate that significant enhancements in joint performance can be achieved using very low pin areal densities (e.g. less than 0.5 %) by selectively placing z-pins at specific positions within the joint; however, the specific role of these localised pins in improving joint performance has yet to be investigated in detail.

Based on these observations, the present study aims to explore, through a combined experimental–numerical analysis, the beneficial effects and the mechanical role of edge-localised, low-density pinning on the structural performance of step-lap joints under tensile loads. Direct observations were performed to characterise the onset and growth of debonding cracks leading to the final separation of the adherends; additionally, finite element (FE) models were developed to assess how the pins modify the interfacial traction field and reduce the energy available to drive damage growth. The experimental findings and numerical results are analysed to clarify the mechanisms through which the pins improve the fracture response of the joints, thereby offering key insights for more efficient and optimised design of z-pinned reinforced connections.

2. Materials and methods

2.1. Experimental

Single-step joints were produced by joining $[90/0]_{2s}$ laminated panels across a 40 mm overlap at the mid-plane $0^{\circ}/0^{\circ}$ interface, without the use of an additional adhesive layer. The base material was a carbon/epoxy pre-preg unidirectional tape (*HS150/ER450*; CIT, Italy), with a nominal ply thickness of 0.15 mm and a weight fiber fraction of 62 %. The joint panels were manufactured by first laying up four $[90/0]_2$ sublaminates, two of which were subsequently trimmed to reduce their length by 40 mm, to accommodate the desired overlap length. Each shortened sublaminate was then stacked onto a full-length one to form an L-shaped adherend with a $[90/0]_{2s}$ layup on the thicker end and a $[90/0]_2$ layup on the thinner end. The two L-shaped adherends were finally flipped and mated together, ensuring precise edge registration and minimal ply-edge clearance so as to prevent the formation of excessively thick resin-rich regions at the bond-line terminations during the cure cycle. Before curing, selected panels were reinforced through the thickness using 0.5 mm diameter stainless steel (AISI 304) pins. The z-pins were obtained from a continuous steel wire that was mechanically abraded to increase surface roughness and improve interfacial adhesion with the composite matrix. For this purpose, the steel wire was axially rotated at 300 rpm and abraded with lubricated 80-grit emery paper, which was moved back and forth along the wire axis to obtain a uniform, cross-hatched surface morphology. Following abrasion, the wire was cleaned using isopropyl alcohol to remove residual lubricant and debris. Post-processing topographical analysis using a non-contact 3D surface profiler (Keyence VHX-X1) indicated a final average surface roughness Ra of approximately 8 μm.

The pins were manually inserted into pre-punched holes created by a 0.5 mm needle. These were arranged in four rows—two per edge—positioned 5 mm from each joint edge. The distance between adjacent pins in each row was 5 mm, and the pin areal density within the overlap region was less than 0.2 %. After insertion, the protruding pin ends were sheared off flush with the surface using a sharp cutter. The choice of a pre-hole equal in diameter to the pins, combined with the use of a 3D-printed fixture to guide pin insertion, enabled accurate alignment of the reinforcing pins and limited the Z-pin misalignment in cured panels to an average of less than 7°, as assessed by X-ray analysis of thin strips cut from the joint panels. It should be noted that the two rows of pins external to the overlap were introduced solely to restrain the potential growth of small delaminations outside the joint region. However, as described in the following sections, the ultimate failure of the joints was invariably controlled by the propagation of interfacial debonding cracks along the overlap region.

Unpinned control panels were also manufactured to provide a baseline for comparison. Both the unpinned and pinned panels were vacuum-bagged and cured in an autoclave for 2 h at 135 °C under a pressure of 6 bar. Thin silicone rubber layers were placed on both surfaces of the z-pinned panels to minimise any misalignments generated by the pressure applied during consolidation [24]. Specimens with a width of 20 mm (Fig. 1) were finally cut from the consolidated panels using a diamond wheel. To ensure high specimen quality, the specimens were microscopically and ultrasonically inspected, confirming a uniform bond-line and negligible void content.

Uniaxial tensile tests were conducted on a 250 kN *Instron* servo-electric testing machine under displacement control at a crosshead speed of 1 mm/min. The applied load and longitudinal strain along the joint overlap (measured using an extensometer with a 62.5 mm gauge length) were continuously recorded to evaluate the stiffness degradation associated with damage initiation and propagation. The initiation and growth of damage leading to final separation were also continuously monitored on both sides of the specimen over the full overlap length using two high-resolution cameras.

2.2. Numerical modelling

A three-dimensional finite element (FE) model, shown in Fig. 2 for the pinned configuration, was developed in *ABAQUS* to investigate the mechanical and fracture responses of the joints examined in the experiments. The composite adherends and the z-pins were discretised using 8-node linear brick elements (C3D8). Each ply was modelled with a single element, resulting in eight elements through the laminate thickness. The pins were modelled as straight and perpendicular to the joint interface, although, as reported previously, a slight average pin misalignment (less than 7°) was measured in the pinned-joint specimens. This assumption constitutes a modelling simplification introduced to reduce mesh complexity and computational expense. Nevertheless, the specific influence of pin misalignment on the structural performance of selectively pinned joints certainly represents a key area for further dedicated investigation. The stress–strain responses of the cured prepreg lamina and the steel wire used for the pins were characterised experimentally through tensile tests to determine the main mechanical properties required for the FE simulations. The composite plies were assumed to be linear elastic, while the behaviour of the z-pins was described by an elasto-plastic constitutive law with isotropic hardening, specified using the experimental stress–strain curve of the source steel wire (Fig. 3) as input.

The interface between the adherends was modelled using a surface-based cohesive contact formulation governed by a bilinear trac-

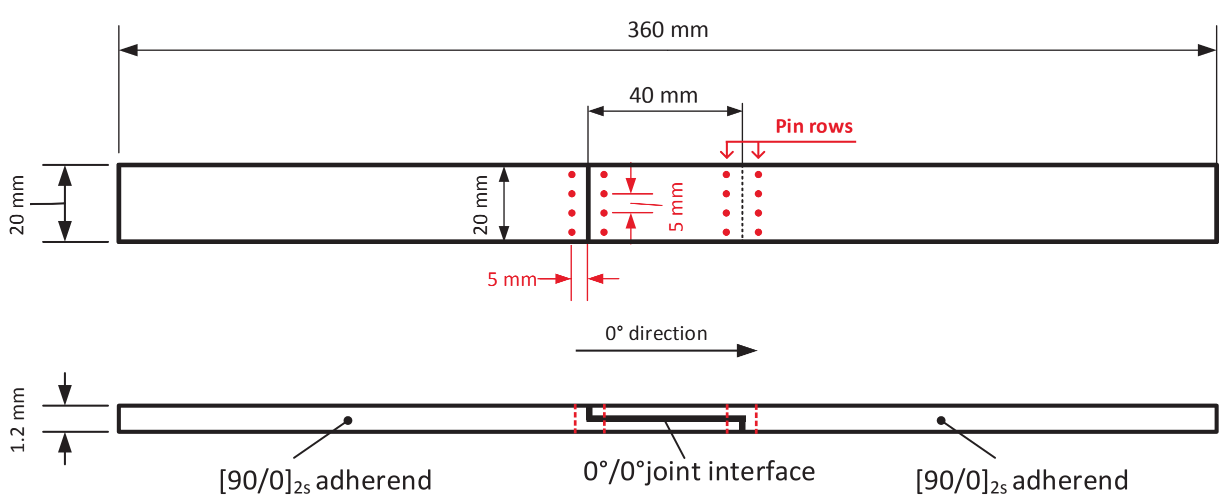

Fig. 1. Geometry of a pinned joint specimen (dimensions not to scale).

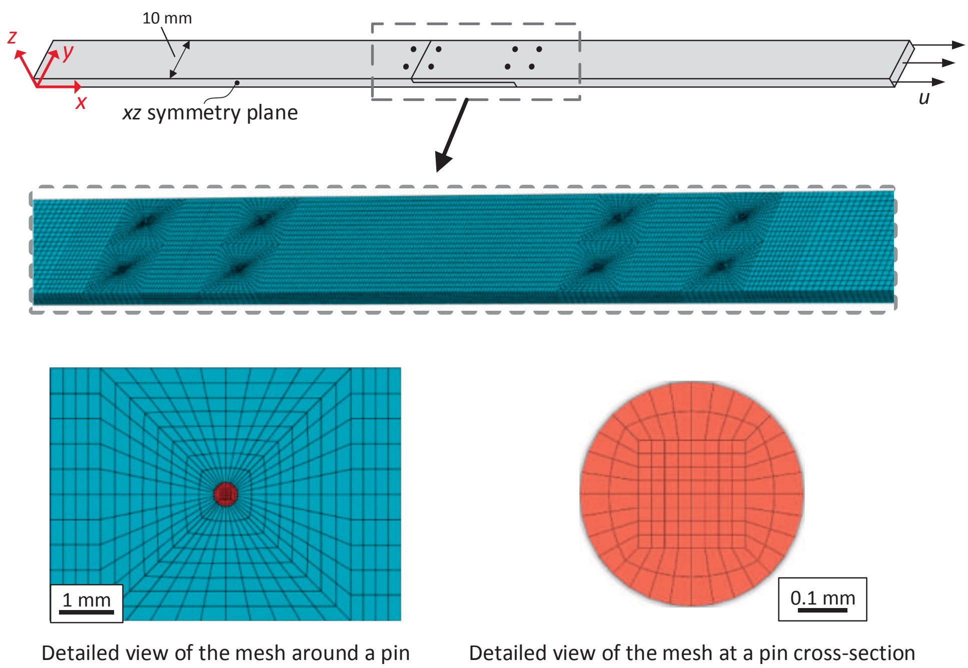

Fig. 2. Finite element model of the z-pinned joint: overall geometry and mesh details around the pin and at a pin cross-section.

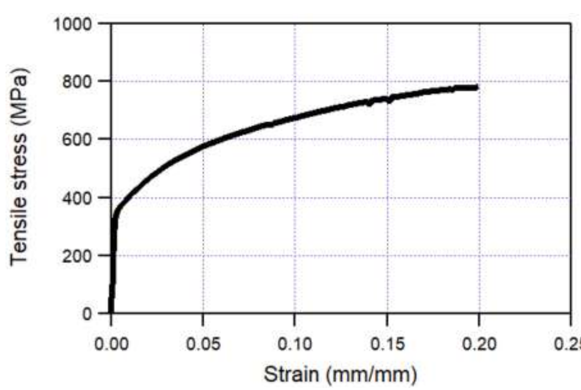

Fig. 3. Experimental stress–strain curve of the steel wire used for the pins.

tion–separation law. A quadratic stress criterion was used to identify the initiation of damage at the joint interface, while damage evolution was controlled by an energy-based law defined in terms of the critical normal and shear fracture energies. Mixed-mode behaviour was accounted for using the Benzeggagh–Kenane criterion [42], which defines the critical fracture energy G^c as a function of mode mixity:

$$G^c = G_n^c + (G_s^c - G_n^c)\left\{\frac{G_s + G_t}{G_n + G_s + G_t}\right\}^{\eta} \tag{1}$$

where, G_n, G_s and G_t denote the normal (G_n) and shear (G_s, G_t) energy release rates, while $G_n^c = G_I^c$ and $G_s^c = G_{II}^c + G_{III}^c$ represent the normal and shear critical fracture energies. G_{III}^c was assumed to be equal to G_{II}^c. The Benzeggagh–Kenane parameter η was set to 2 in accordance with the value indicated in [43] for a toughened carbon/epoxy material. A sensitivity study revealed, however, that the influence of the η parameter is negligible, as debonding propagation is predominantly controlled by mode II loading.

Following the onset of damage, the decohesion of the interface progresses as the separation increases, with complete failure occurring when the energy dissipated during separation reaches the critical fracture energy G^c. A damage variable, d, ranging from 0 (no damage) to 1 (complete decohesion), is used to represent the evolution of damage at the interface. A Coulomb friction model, with a friction coefficient of 0.2 [44], is included in the contact formulation to simulate the potential interaction between the adherends after complete separation.

The in-plane elastic properties of the cured unidirectional layer were determined experimentally using specimens with stacking sequences $[0]_{10}$, $[90]_{10}$ and $[+45/\text{-}45]_{2s}$. All specimens were instrumented with longitudinal and transverse extensometers to measure the corresponding strain components during testing. The longitudinal modulus E_x and the transverse modulus E_y were respectively obtained from tensile tests on $[0]_{10}$ and $[90]_{10}$ laminate specimens, performed according to [45]. The Poisson's ratio ν_{xy} was evaluated from simultaneous longitudinal and transverse strain measurements during the tensile tests on the $[0]_{10}$ specimens. The in-plane shear modulus G_{xy} was determined from tensile tests on the $[+45/-45]_{2s}$ specimens following [46]. The out-of-plane elastic constants were defined by assuming transverse isotropy in the y–z plane. The through-thickness elastic modulus E_z and out-of-plane shear modulus G_{xz} were assumed to be equal to their in-plane counterparts. The transverse Poisson's ratio ν_{yz} was set to 0.30—higher than the measured $\nu_{xy} = 0.26$ —to account for the resin-dominated response and lower fibre constraint in the transverse plane.

The critical interlaminar fracture energies in mode I (G_I^c) and mode II (G_{II}^c) were obtained experimentally from Double Cantilever Beam (DCB) and End-Notched Flexure (ENF) tests, conducted on unidirectional samples according to ASTM standards [47,48]. FE simulations of DCB and ENF tests were performed to calibrate the interfacial strength (t_n^0, t_s^0, t_t^0) and stiffness (k_n, k_s, k_t) parameters through comparison with the experimental force–displacement curves. The composite arms and the middle interface of the samples were respectively modelled using the same elements and surface-based cohesive formulation adopted for the joint simulations. For the DCB case, the nodes at one end of the laminate were fully constrained, while the opening displacement was applied to the opposite arm through the loading nodes. For the ENF case, the laminate was supported by two rollers and subjected to a prescribed displacement through the upper loading roller, reproducing the experimental three-point bending configuration. Contact interactions were defined between the delaminated arms and between the specimen and the loading/support rollers, which were modelled using R3D8 rigid elements. The mesh geometry adopted for the DCB and ENF models is shown in Fig. 4a. Elements with a size of 0.5 mm along the axial direction provided converged solutions in a mesh sensitivity analysis. The experimental DCB and ENF curves, together with the FE simulated responses predicted using the identified interfacial cohesive parameters, are presented in Fig. 4b and c.

The complete set of elastic, strength, and cohesive properties adopted in the simulation of the joints is listed in Tables 1 and 2.

To simplify the numerical modelling, the local resin-rich pocket around the pins was not explicitly discretised; instead, the mechanical behaviour of the pin–laminate interface was represented using a cohesive interface formulation. As a baseline assumption, in the absence of specific experimental data for the pin–resin bonding, this interface was modelled using the same properties adopted for the interface between the composite adherends. Furthermore, the resin-rich region between the ends of the adherends was likewise modelled using a cohesive law.

The boundary conditions applied to the model are illustrated in Fig. 2. The specimen was fully constrained at one end (plane *y-z*), whereas displacements *u* were imposed in the *x*-direction at the opposite end to reproduce the movement of the testing machine crosshead. Applying symmetry conditions on the *x-z* plane, only half of the specimen (with a width of 10 mm) was modelled, thereby reducing computational costs. The final mesh density was established through a sensitivity study, to ensure the convergence of the numerical solution. An interfacial-element size of 0.25 mm along the axial direction—with the mesh locally refined in the vicinity of the pins (see the detailed view in Fig. 2)—was found to provide stable results with respect to further mesh refinement.

The *Abaqus/Explicit* solver was employed for the numerical simulations, utilising a mass scaling factor of 1000 to reduce execution time. This factor was determined through a sensitivity study to verify that the kinetic energy remained below a threshold of 2 % of the internal energy throughout the analysis.

Table 1
Elastic properties of the cured carbon/epoxy prepreg material.

E_x (GPa)	$E_y = E_z$ (GPa)	$G_{xy} = G_{xz}$ (GPa)	G_{yz} (GPa)	$\nu_{xy} = \nu_{xz}$	ν_{yz}
120	8.2	4.0	3.2	0.26	0.3

Table 2
Fracture properties of the 0°/0° joint interface.

Stiffness $k_n = k_t = k_s$(GPa/mm)	t_n^0(MPa)	$t_s^0 = t_t^0$(MPa)	G_I^C(J/m^2)	G_{II}^C(J/m^2)
1E14	30	60	506	710

3. Experimental results

Fig. 5 presents representative load per unit width versus strain curves of unpinned and z-pinned joints measured during quasi-static tensile tests. Both joints exhibit a linear initial load–strain response, characterised by practically identical initial stiffness during the early stages of loading. As the applied displacement increases, the curves progressively deviate from linearity, showing a reduction in stiffness associated with

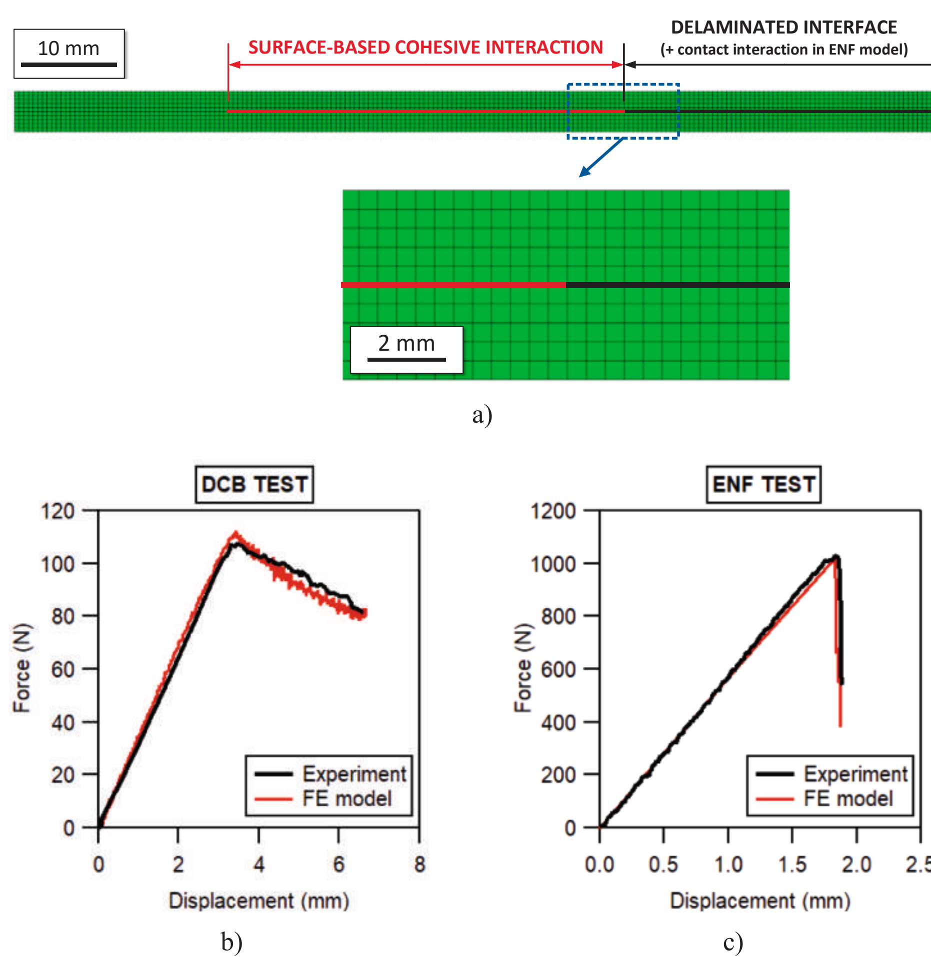

Fig. 4. Finite element modelling of DCB and ENF tests: mesh used for the numerical analyses (a), and comparison between experimental and FE-predicted responses for the DCB (b) and ENF (c) tests using the material properties reported in Tables 1 and 2.

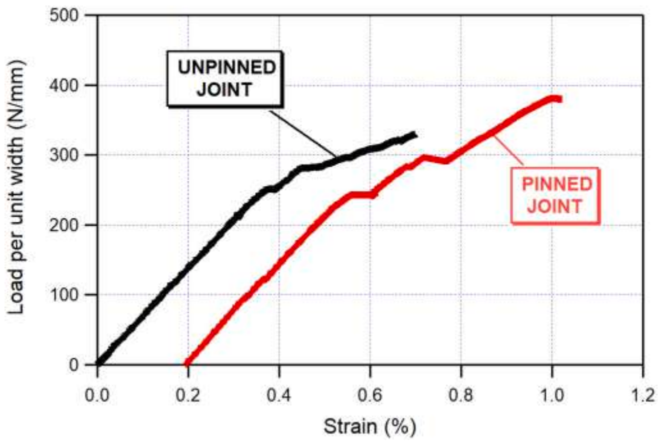

Fig. 5. Load per unit width versus strain for unpinned and z-pinned joints. The curve for the z-pinned joint is shifted for clarity.

the initiation and growth of damage at the edges of the joint.

Unpinned and pinned joints exhibit a similar sequence of damage events leading to final failure (Fig. 6). Initially, small matrix cracks occur in the resin-rich regions between the ends of the adherends at a load of approximately 100 N/mm. These cracks do not affect joint stiffness, but act as stress concentrators, triggering the onset of debonding cracks at both ends of the joint (Fig. 6a) once the strain exceeds a value of approximately 0.4 %. With increasing strain, the debonding cracks grow from the joint edges toward the centre of the overlap (Fig. 6b and c). As final failure approaches, one crack advances more rapidly than the other, becoming the dominant crack whose unstable propagation ultimately drives the complete separation of the adherends. Direct observations conducted during the tests revealed no signs of premature pin pullout. Microstructural analysis of the failed surfaces indicated that the z-pins remained intact after joint failure, with no broken pins detected. Instead, the pins underwent large plastic shear deformation as a result of the high loads sustained during the final stages of adherend separation and were finally pulled out from one of the adherends (Fig. 7). No evident matrix cracking or fiber damage was observed within the adherends after separation, indicating that the primary damage—alongside the plastic deformation of the pins—was limited to the joint interface and the pin–matrix interface.

The load–strain curves in Fig. 5 show that the z-pinned joints achieve higher stress and strain at failure than the unpinned joints, demonstrating the beneficial effect of z-pins on both strength and damage tolerance. The ultimate strengths and failure strains of the tested

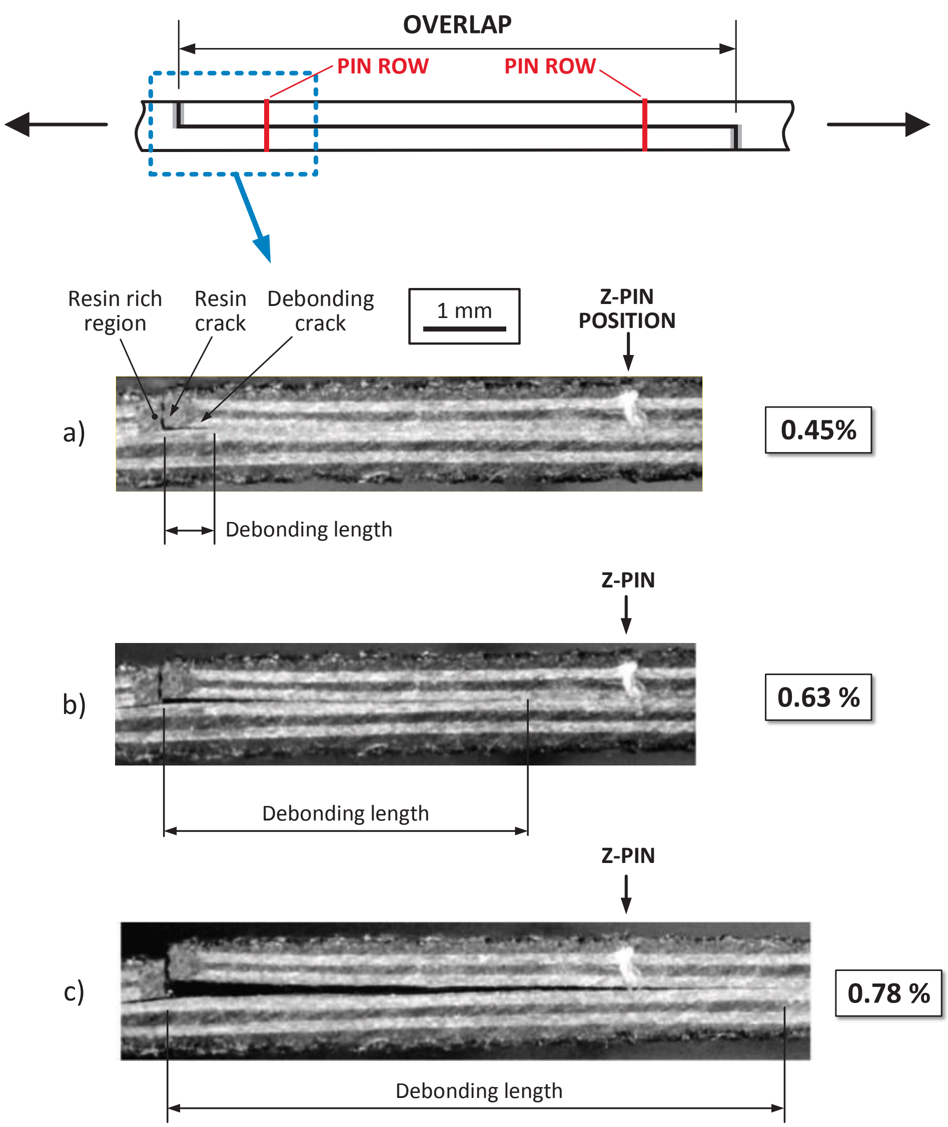

Fig. 6. Initiation and growth of a debonding crack at the joint edge of a pinned joint. The labels indicate the strain levels.

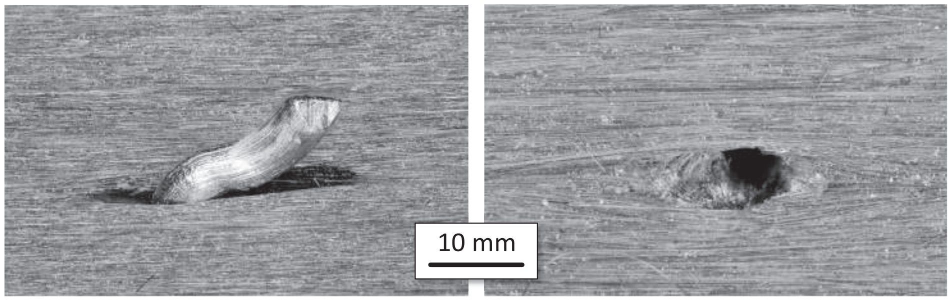

a) b)

Fig. 7. Plastically deformed pin (a) and corresponding pin hole in the mating adherend (b) after separation.

samples are reported in Table 3, while a direct comparison of the average values of the initial stiffness, strength, and failure strain of the two classes of joints is presented in the graphs of Fig. 8. These data indicate that, while pins play no significant role in the early loading stage, they clearly enhance the ultimate load-carrying capacity and damage tolerance of the joints, with average increases of about 16 % in strength and 25 % in strain at failure, respectively, compared with the unpinned joints.

Fig. 9 shows typical evolutions of the average length of the interfacial debonding cracks as a function of strain for both unpinned and pinned joints. The average crack length was evaluated as the sum of the crack lengths measured at the two joint edges, thereby accounting for damage propagation from both ends of the overlap. The crack length at each joint edge was calculated by averaging the measurements taken on both sides of the specimen from images acquired with cameras during testing. At both edges, the crack lengths measured on the two sides of the specimen were comparable, with differences generally within 15 %, indicating that the crack front remained reasonably uniform across the joint width during propagation. The average crack lengths at the two edges of the joint were also similar until, as ultimate failure approached, the crack at one edge advanced much faster than the other, leading to the rapid and complete separation of the joint.

The crack growth data indicates that, while interfacial debonding initiates at a similar strain level for both joints, crack propagation is significantly slower in pinned joints. Of particular interest, the capacity of the pins to retard crack growth becomes effective well before the crack front reaches the pin rows, which are located 5 mm from the joint edges. This behaviour suggests that z-pins contribute to toughening not only through the well-known bridging effect —which develops once the crack front has advanced beyond the pin rows—, but also through a shielding mechanism. By altering the stress field ahead of the crack tip, this mechanism delays crack propagation during the early stages of debonding while the crack front is still behind the pin rows, as will be numerically investigated in the following section. A further characteristic of the crack data in Fig. 9 is the contrast in the trends of growth rates. In unpinned joints, the crack growth rate increases in a relatively steady manner with strain. Conversely, as the crack in the pinned joints approaches the pin row, it undergoes an abrupt jump, quickly reaching and extending beyond the pins, thereby activating the bridging mechanism of the transverse reinforcement.

Table 3
Strength and failure strain of tested joint specimens.

Joint type	Specimen ID	Strength (MPa)	Strain at Failure (%)
UNPINNED	U1	292	0.581
	U2	302	0.639
	U3	305	0.736
	U4	319	0.690
	U5	330	0.696
	Average	309.6	0.668
	(± SD)	(±14.9)	(±0.060)
PINNED	P1	342	0.770
	P2	348	0.833
	P3	350	0.832
	P4	377	0.925
	P5	381	0.809
	Average	359.6	0.834
	(± SD)	(±18.0)	(±0.057)

To allow a direct comparison between the damage progression and the structural response of the joints, the crack growth data are plotted in Fig. 10 alongside the load–strain curves for both the unpinned and z-pinned joints. As expected, the plots show that the onset of non-linearity in the load–strain response beyond a certain strain level is directly related to the initiation and propagation of interfacial debonding at the joint overlap ends.

4. Numerical results and discussion

4.1. FE predictions of pinned and unpinned joint behaviour

Fig. 11 compares the predictions obtained through FE analysis with the experimental load–strain curves for both unpinned and pinned joints. The results show good agreement between the numerical simulations and the experimental data, with the model accurately capturing the transition from the linear elastic to the non-linear regime and correctly reproducing the subsequent debonding-controlled response. In particular, as summarised in the graph of Fig. 12, the FE model closely predicts the enhancement in both peak strength and failure strain induced by the presence of z-pins.

The FE model is also capable of reproducing the characteristic trends of interfacial debonding growth observed during the static tests in the two classes of joints. The graphs in Fig. 13 compare the evolution of the cohesive zone predicted by the FE analyses with the debonding lengths measured during the tests. The FE data provides the sums of the distances from the joint edges of the characteristic fronts of the process zones: the first corresponding to the onset of cohesive softening (damage initiation, $d = 0$) and the second to the complete decohesion (interface failure, $d = 1$). The region enclosed between these two curves (shaded in the graphs) thus represents the cohesive process zone, i.e. the portion of the interface where damage is accumulating ($0 < d < 1$), and its evolution with increasing strain provides insight into the growth of interfacial debonding. It can be seen that good quantitative agreement is achieved between the progression of debonding predicted by the model and that observed experimentally for the two joint types. In unpinned joints, the FE model correctly simulates a cohesive debonding zone that moves at a steadily increasing rate with rising strain until it becomes unstable, leading to complete joint separation (Fig. 13a).

In pinned joints, by contrast, numerical results indicate that upon reaching a certain strain level the cohesive zone undergoes a sudden jump and then propagates past them resuming a stable growth up to final failure. The abrupt growth of the debonding crack is a distinctive

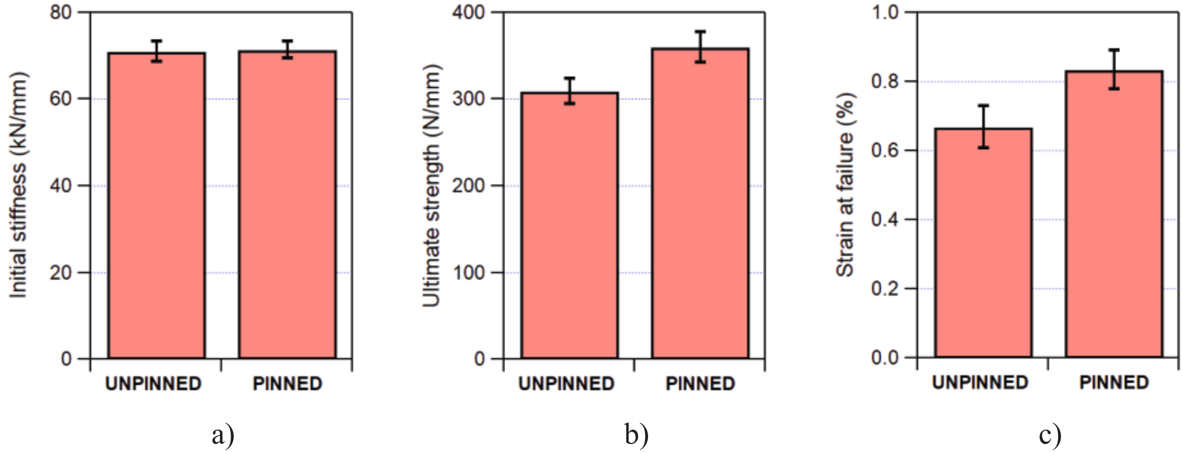

Fig. 8. Comparison of initial stiffness (a), ultimate strength (b), and strain at failure (c) for unpinned and z-pinned joints. The error bars represent ± one standard deviation.

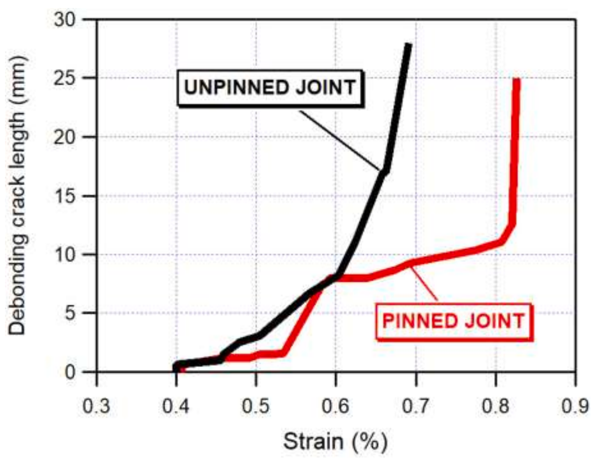

Fig. 9. Typical evolution of debonding crack length in unpinned and z-pinned joints.

feature characterising the behaviour of pinned joints and is clearly visible in the experimental data plotted in Fig. 13b. The FE model successfully captures this sharp jump, although its onset is predicted at a slightly higher strain than that observed experimentally.

Fig. 14 shows the outlines of the deformed shapes of a pinned joint in the vicinity of the edge, as obtained from the FE analysis at the same strain levels of the cracked configurations presented in Fig. 6. The simulation captures the sequence of damage evolution, where interfacial debonding is triggered by a matrix crack in the resin pocket at the overlap boundaries. With increasing strain, the debonding crack grows inward, reaching the pin rows and continuing beyond them towards the centre of the overlap. It is observed that, as the crack length increases, the relative sliding between the debonded adherends becomes more pronounced, inducing progressive tilting of the bridging pins and leading to high-pressure contact with the laminate wall; this contact state drives the snubbing effect [49], thereby increasing the frictional resistance to pull-out and promoting pin retention within the adherends. As a result, pin pull-out is deferred and, as observed experimentally, the pins undergo severe plastic shear deformation upon complete joint separation (see Fig. 7). Fig. 14 also shows the spatial distribution of cohesive damage at the pin–laminate interface for the three examined strain levels. The FE results indicate that damage at the pin–laminate interface initiates at relatively low strain levels. With increasing strain, the damage propagates along the interface, eventually extending over most of the pin–laminate interface area before ultimate joint failure. Despite the extensive damage at the pin–laminate interface, the z-pins continue to contribute to load transfer between the adherends through their shear deformation, while pull-out is inhibited, as experimentally observed,

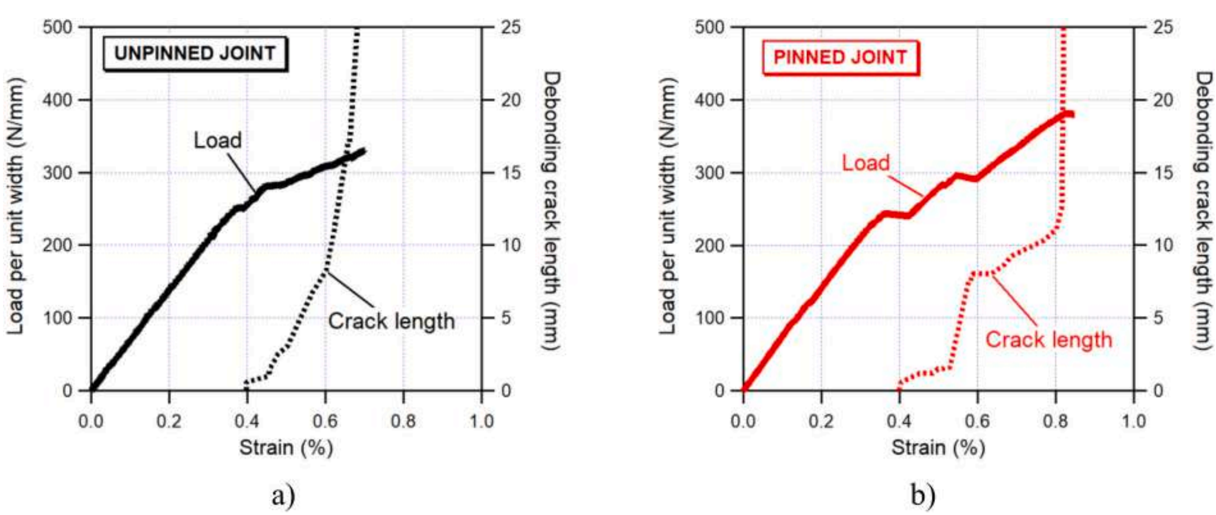

Fig. 10. Load and debonding crack length as a function of strain for (a) unpinned and (b) z-pinned joints.

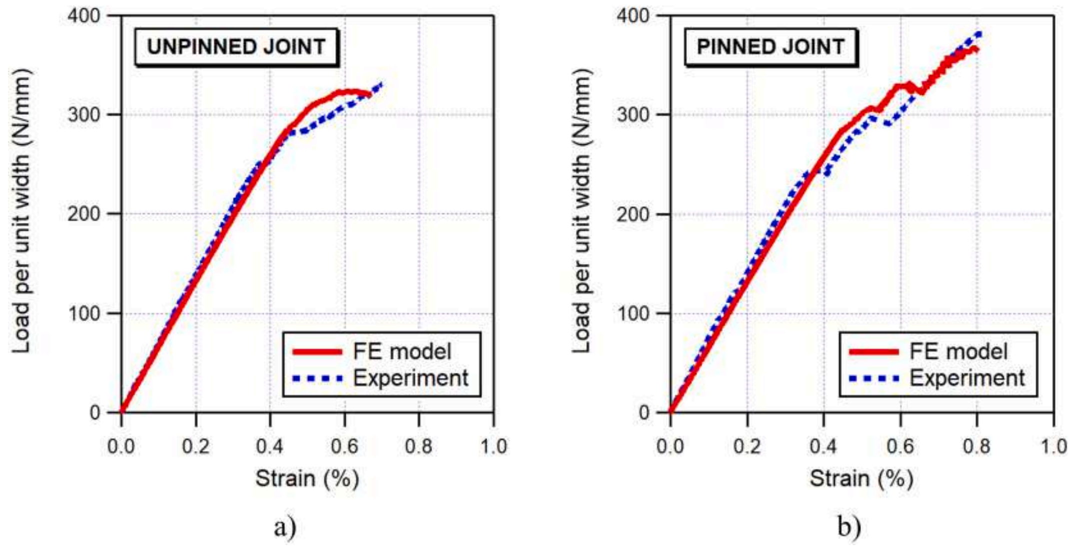

Fig. 11. Comparison of experimental and numerically predicted load vs. strain curves for unpinned (a) and z-pinned (b) joints.

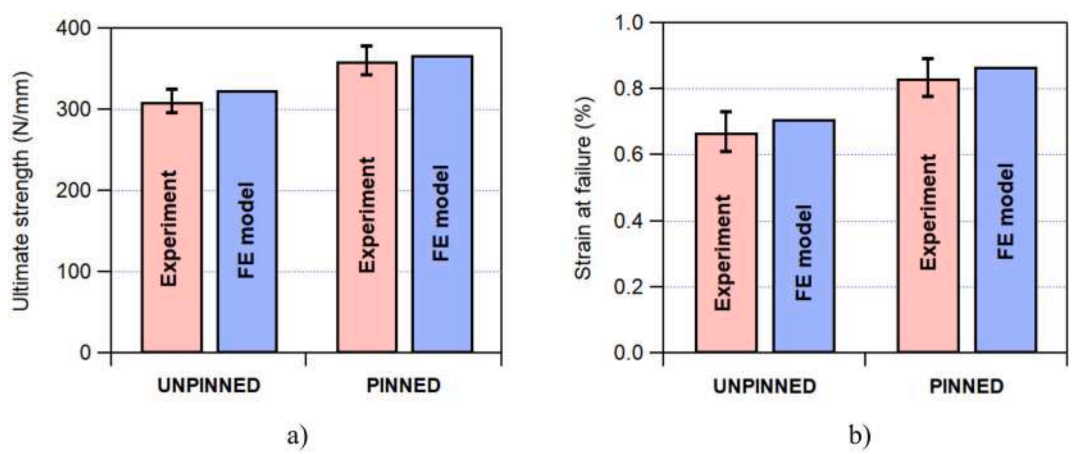

Fig. 12. Comparison of experimental and numerically predicted ultimate strength (a) and strain at failure (b) for unpinned and z-pinned joints. The error bars represent ± one standard deviation.

due to the predominance of Mode II loading and the frictional resistance generated by the snubbing mechanism.

4.2. Interfacial stress analysis

Further insight into the toughening mechanisms introduced by the pins may be gained by analysing the FE stress data at the joint interface. It should first be noted that shear stresses dominate over normal stresses as soon as cohesive damage is initiated at the joint edge (see, for example, the graphs in Fig. 15, which report the stress distributions for a strain level of 0.35 %, corresponding to a process zone of about 1 mm). Consequently, the following discussion is focused on the analysis of shear stress distributions, as they play the dominant role in driving the interfacial fracture response and, ultimately, the structural performance of the joint. It is worth recalling, however, that the cohesive formulation adopted in the simulations explicitly accounts for the effects and interaction of shear and normal stresses in governing the onset and evolution of interfacial debonding, as detailed in Section 2.2.

The plots in Fig. 16 illustrate the evolution of interfacial shear stress with strain level, as extracted from the FE output at three distances from the joint edge (0.5, 1.5, and 3 mm) along a longitudinal line passing through a pin. The FE results reveal that at locations close to the edge of the joint (Fig. 16a, distance from joint edge = 0.5 mm), the initial elastic response and a substantial fraction of the softening branch follow an identical trajectory in unpinned and pinned joints. At a strain level of approximately 0.45 %, the shear stress of the unpinned joint exhibits a rapid drop to zero, resulting in complete interface decohesion; in contrast, the interface of the pinned joints remains in a partially damaged state, with the shear stress stabilised at an almost constant value up to a much higher strain level (over 0.6 %). Analogous trends are observed at a distance of 1.5 mm from the joint edge (Fig. 16b), even though the common trajectory shared by the unpinned and pinned joints during the softening stage is now significantly reduced. As the position of the pin is further approached (distance from joint edge = 3 mm; Fig. 16c), the divergence between the interface behaviour of unpinned and pinned joints becomes increasingly pronounced. In this case, the shear stress at the interface of the pinned joint deviates from that of the unpinned counterpart while still in the elastic regime. With the stress nearing the 0.45 % strain value, the shear stress of the unpinned joint increases sharply until the initiation of decohesion, at which point it rapidly completes the degradation phase; in contrast, the shear stress of the pinned joint remains within the elastic regime up to a strain exceeding 0.6 %, and only beyond this strain does the stress rises abruptly, leading to unstable behaviour and eventual complete interfacial failure.

The FE results demonstrate that the pins exert a notable effect on the

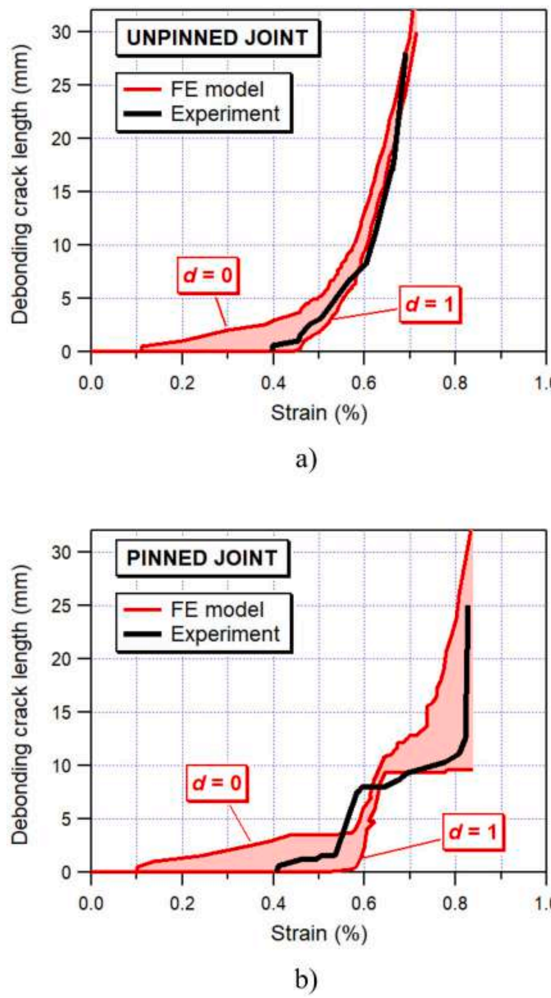

Fig. 13. Comparison of experimental and numerically predicted evolution of the debonding crack with strain for unpinned (a) and z-pinned (b) joints. The FE simulation results show the evolution of the interface cohesive process zone, where $d = 0$ corresponds to the initiation of damage and $d = 1$ to complete decohesion.

interfacial behaviour well before the cohesive process zone reaches the pin row. The presence of pins delays the initiation and progression of decohesion, maintaining the interface in an elastic or partially damaged condition over a wider strain range than in unpinned joints. The restraining effect on damage progression is weak at a distance from the pin row but becomes increasingly pronounced as the cohesive front nears the pins. This results in a stabilisation of the debonding process, deferring the transition to unstable propagation and contributing to the improved joint strength and failure strain observed in the experimental tests.

The redistribution of stress generated at the joint edge by the pins is presented in the graphs of Fig. 17, which show the profiles of the interfacial shear stress along the overlap for three strain levels. At a strain of 0.44 % (Fig. 17a), the shear stress field in the vicinity of the joint edge remains similar in both pinned and unpinned joints; closer to the pins, however, the stresses in the pinned joints become significantly higher than those in the unpinned counterparts. This effect is due to the local stiffening mechanism of the pins, which restrain the relative displacements between the adherends and modify the load transfer path through the joint. The local redistribution of interfacial shear stresses induced by the pins exerts a shielding effect on the front of the cohesive region, thereby limiting the energy available for the progression of decohesion and the advancement of the process zone. Fig. 17 demonstrates that, while an increase in the applied strain from 0.44 % to 0.5 % triggers significant propagation of the process zone in unpinned joints (Fig. 17b and c), the cohesive zone remains stationary in pinned joints.

The abrupt growth of the debonding crack that characterises the response of the pinned joints is driven by the sudden release of strain energy after the phase of stable pin-induced shielding. The FE results plotted in Fig. 13b show that, up to a strain of almost 0.6 %, the pins effectively shield the crack tip, keeping the cohesive zone stably confined to a small region (approximately 2 mm long) at the joint edge. However, as seen in the graphs of Fig. 16, the load increments applied from strain levels above 0.45 % are increasingly carried by the narrow, residual elastic ligaments just ahead of the pins. This causes rapid shear strain localisation and a sharp increase in the Mode II crack driving force. Once these remaining ligaments fail, the stored elastic energy is abruptly released, driving the rapid advance of the crack towards the pin row.

It should also be noted that slight irregularities along the bond-line interface may cause crack propagation to occur in small, discrete steps, as observed at a strain of approximately 0.4 % in the experimental response of the unpinned joint (Fig. 10a). As the FE model assumes a perfectly uniform interface, these minor crack-growth increments cannot be reproduced in the numerical simulations (Fig. 11a). Nevertheless, the FE model captures the stepwise changes in the force–strain response of the pinned joint observed at strains above 0.5 % (Fig. 11b), which are associated with the major, sudden crack advancements that marks the transition from the shielding phase to the bridging mechanism.

To further assess the efficacy of the shielding effect, the local energy dissipation was evaluated and compared between pinned and unpinned joints at equivalent overall strain levels. The dissipated energy was extracted from the nodes of the cohesive interface at specific coordinates along the overlap length to map the influence of the pin-to-node distance.

The dissipated energy density G was calculated at the front of the cohesive zone using the following definition:

$$G = \int_0^{\overline{u}} \tau(u)du - U_e(\overline{\delta})$$

where τ is the interfacial shear stress, u is the corresponding relative displacement at the cohesive interface, and $U_e(\overline{u})$ is the recoverable elastic energy density associated with the current degradation state. To ensure a meaningful comparison, the energy dissipations in the unpinned and pinned joints were sampled at the same strain level, chosen to correspond to the state immediately prior to the onset of complete decohesion in the unpinned joints. As previously mentioned, normal stresses play a minor role in the crack growth process, and therefore only interfacial shear stresses were considered in the calculations. To quantify the shielding effect, the dissipated energy densities were normalised against the unpinned baseline ($G_{pinned}/G_{unpinned}$). These ratios are plotted in Fig. 18 for the region spanning from the joint edge to the pin row, mapping the local shielding effectiveness of the through-thickness reinforcement.

The graph provides immediate evidence of the pin-induced reduction in the energy spent for interfacial degradation at equivalent strain levels, while also offering insight into the spatial range of the shielding provided by the pins. Near the edge of the joint, the ratio remains relatively close to unity, indicating that the pins, due to their distance, do not yet exert a marked influence on stress distribution and associated damage evolution, thereby yielding only a limited shielding effect in this region. However, as the distance between the cohesive front and the z-pins decreases, the ratio drops sharply, demonstrating that the z-pins significantly reduce the energy dissipation demand on the interface. The null values of the ratio near the pins indicate that, under the same applied strain, the interface of the pinned joints remains within the

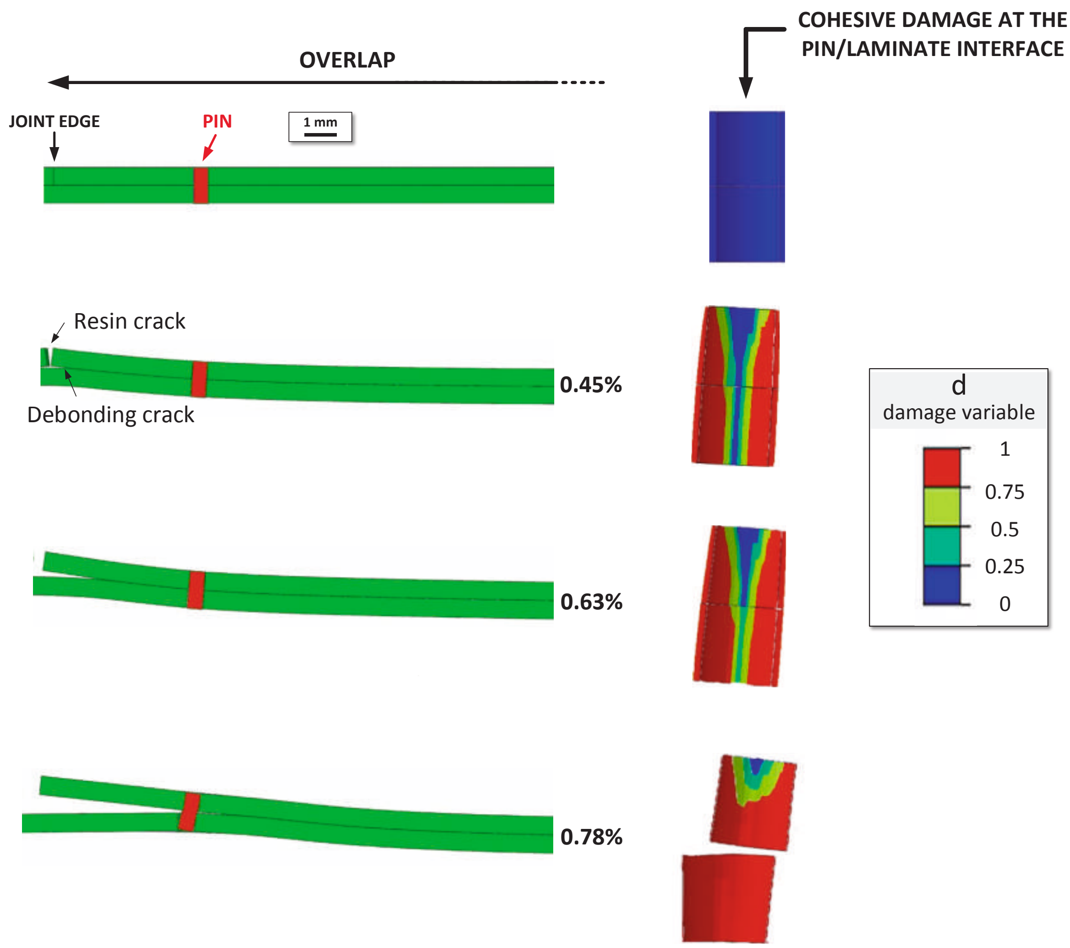

Fig. 14. Outline of the deformed joint edge and cohesive damage at the pin-laminate interface, as predicted by the finite element model at different strain levels (displacements are amplified for clarity).

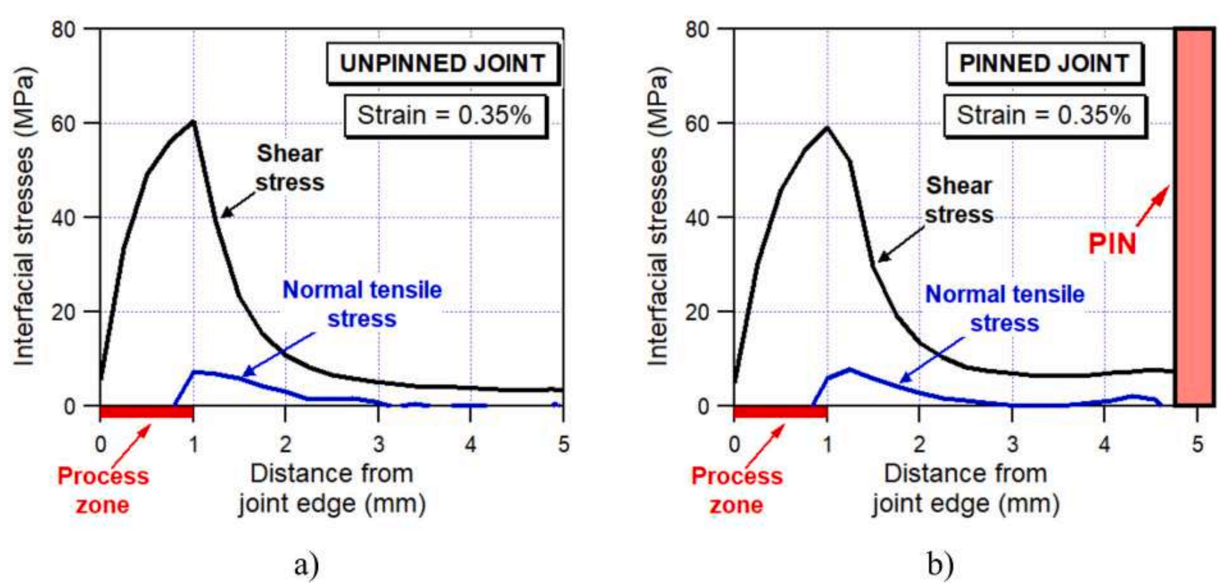

Fig. 15. Interfacial shear and normal tensile stresses predicted by the FE simulations for unpinned (a) and z-pinned (b) joints at a strain level of 0.35 %.

elastic regime when the unpinned joints have already reached complete decohesion, as for example visible in Fig. 16c. The accumulation of irreversible damage at the interface of pinned joints is therefore delayed, thereby maintaining a higher degree of interfacial structural integrity over a significantly wider range of strains compared to the unpinned joints. Only with further increases in strain does the process zone at the edge of the pinned joint become unstable, rapidly extending beyond the pin row and leading to a transition in the pin-induced toughening action

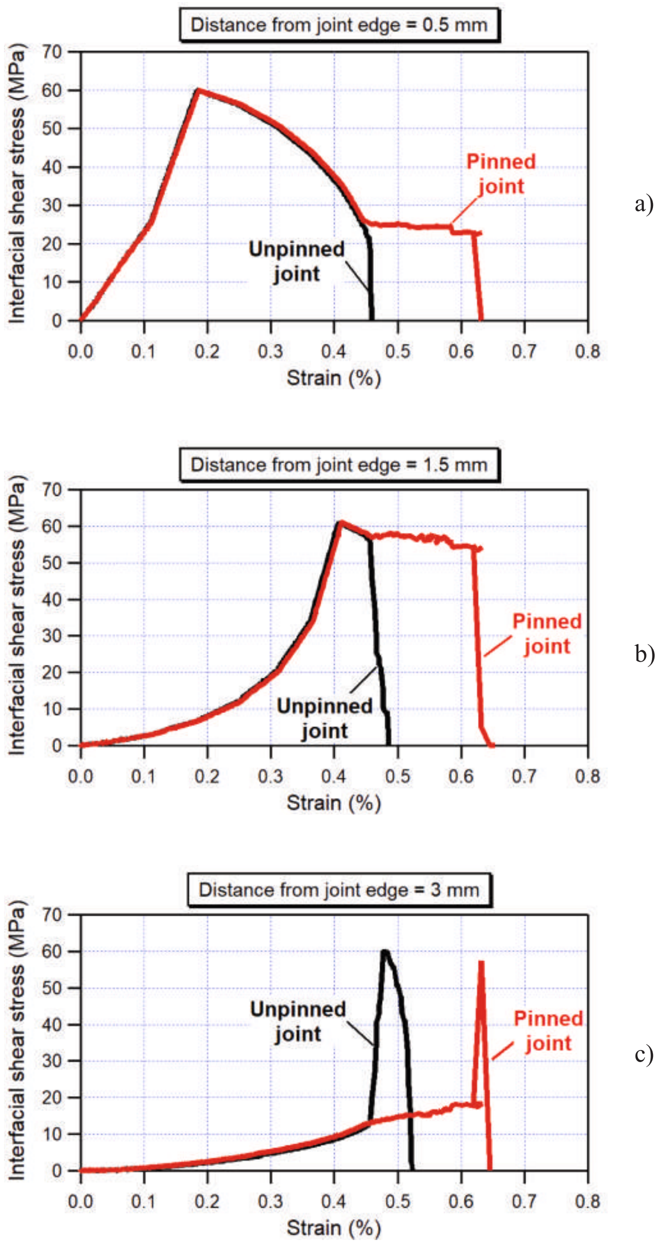

Fig. 16. Comparison of interfacial shear stress vs. strain at different distances from the joint edge, as predicted by the FE simulations for unpinned and z-pinned joints.

from a shielding mode to a bridging mechanism. At this stage, the shielding effect ceases, and the toughening role is assumed by a bridging action in which the pins begin to act progressively as discrete connecting elements that transfer load across the debonded adherends and restrain relative interfacial displacement. The ultimate failure of the pinned joint eventually occurs when the cohesive process zone undergoes unstable propagation under the imposed strain.

5. Conclusions

The study investigated the mechanical performance and damage evolution of single-step composite joints reinforced with the introduction of edge-localized steel z-pins. The mechanical role of z-pins in controlling the growth of damage was examined through a combination of experimental analyses and finite element simulations.

The key findings of this study are summarised as follows:

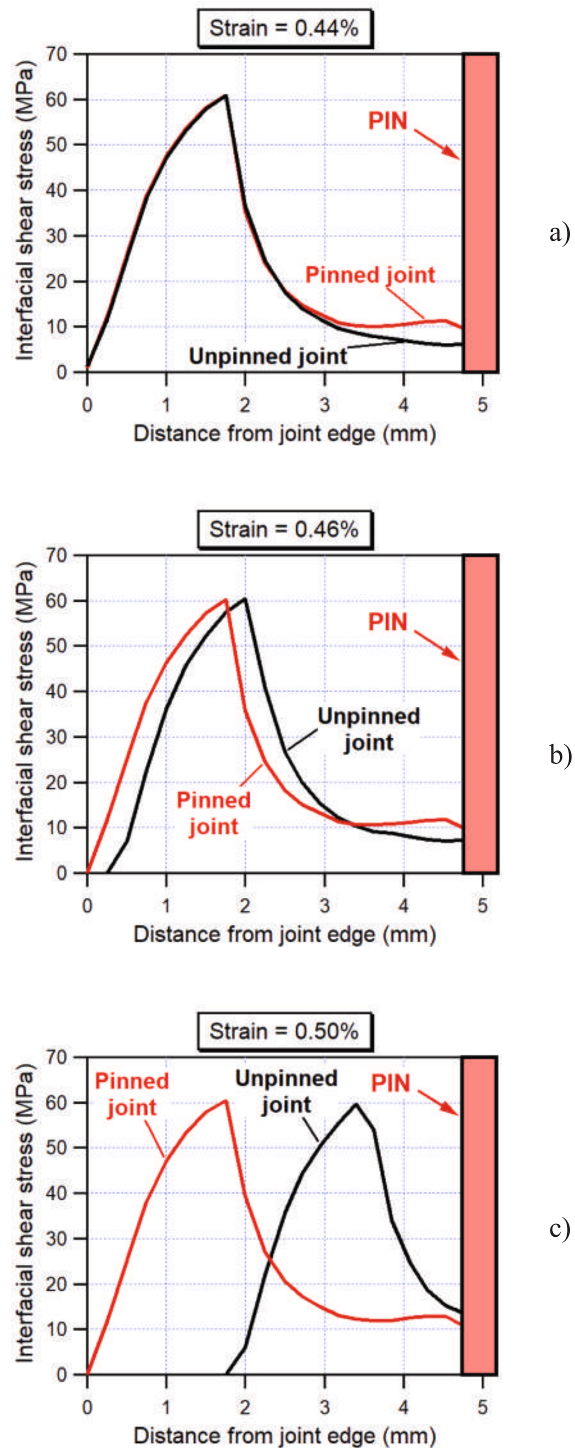

Fig. 17. Comparison of interfacial shear stress at different strain levels, as predicted by the FE simulations for unpinned and z-pinned joints.

- The introduction of z-pins enhances the load-carrying capacity and damage tolerance of the joints, with increases of approximately 16 % in ultimate strength and 25 % in strain at failure. Ultimate failure is driven by the growth of edge cracks that propagate towards the centre of the overlap, until their unstable propagation leads to final separation.
- While interfacial debonding initiates at similar strain levels in both joint types, the presence of z-pins significantly reduces crack propagation rates, delaying crack growth and extending the stable damage evolution phase to higher strain levels.

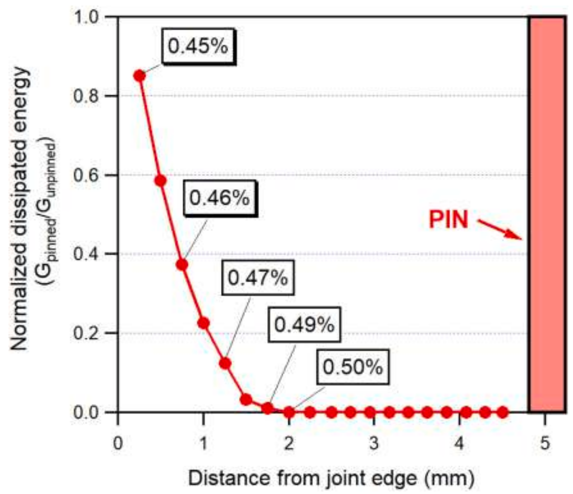

Fig. 18. Ratios of energy dissipated at the tip of the cohesive zone for pinned versus unpinned joints, as predicted by FE simulations at equivalent strain levels (as indicated in the labels).

- Visual inspection during testing showed no evidence of premature pin pull-out, while microstructural observations indicated that the z-pins did not fracture but instead underwent extensive plastic shear deformation during adherend separation.
- The FE simulations show that the pins operate through a dual-stage toughening process:
  - An initial shielding mechanism is established before the cohesive zone reaches the pin row, redistributing interfacial shear stresses ahead of the crack front. This mechanism reduces the energy available for debonding growth, thereby delaying its propagation.
  - A bridging mechanism is subsequently activated once the crack front moves beyond the pins. In this stage, the tractions exerted by the pins across the debonding crack directly restrain the relative displacements of the joint surfaces.
- The results demonstrate that selective, edge-localised pinning is an effective, weight-efficient strategy for enhancing the structural integrity and damage tolerance of composite connections.
- Future work should focus on assessing the effects of the modelling simplifications adopted in the present study, such as the assumption that the pins are perfectly perpendicular to the joint interface and the representation of the resin-rich region surrounding the pins through a cohesive interface.

CRediT authorship contribution statement

G. Loi: Writing – review & editing, Writing – original draft, Methodology, Investigation, Formal analysis, Conceptualization. **F. Aymerich:** Writing – review & editing, Writing – original draft, Methodology, Investigation, Formal analysis, Conceptualization.

Declaration of competing interest

The authors declare that they have no known competing financial interests or personal relationships that could have appeared to influence the work reported in this paper.

Data availability

Data will be made available on request.

References

[1] Tong L, Soutis C. Recent Advances in Structural Joints and Repairs for Composite Materials. Dordrecht: Springer; 2003.
[2] Camanho P, Tong L, editors. Composite joints and connections. Principles, modelling and testing. Cambridge (UK): Woodhead Publishing; 2011.
[3] Budhe S, Banea MD, de Barros S, da Silva LFM. An updated review of adhesively bonded joints in composite materials. Int J Adhes Adhes 2020;72:30–42. https://doi.org/10.1016/j.ijadhadh.2016.10.010.
[4] Shishesaz M, Hosseini M. Effects of joint geometry and material on stress distribution, strength and failure of bonded composite joints: an overview. J Adhes 2018;96(12):1053–121. https://doi.org/10.1080/00218464.2018.1554483.
[5] Kim JK, Mai YW (Editors). Engineered Interfaces in Fiber Reinforced Composites, 1998, Elsevier, Oxford.
[6] Tong L, Mouritz AP, Bannister MK, Mk.. 3D fibre reinforced polymer composites. Oxford: Elsevier; 2002.
[7] Dell'Anno G, Treiber JWG, Partridge IK. Manufacturing of composite parts reinforced through-thickness by tufting. Rob Comput Integr Manuf 2016;37:262–72. https://doi.org/10.1016/j.rcim.2015.04.004.
[8] Daelemans L, van der Heijden S, De Baere I, Rahier H, Van Paepegem W, De Clerck K. Damage-resistant composites using electrospun nanofibers: a multiscale analysis of the toughening mechanisms. ACS Appl Mater Interfaces 2016;8(18):11806–18. https://doi.org/10.1021/acsami.6b02247.
[9] Herráez M, Pichler N, Botsis J. Improving delamination resistance through tailored defects. Compos Struct 2020;247:112422. https://doi.org/10.1016/j.compstruct.2020.112422.
[10] Lubineau G, Alfano M, Tao R, Wagih A, Yudhanto A, Li X, et al. Harnessing extrinsic dissipation to enhance the toughness of composites and composite joints: a state-of-the-art - review of recent advances. Adv Mater 2024;36:2407132. https://doi.org/10.1002/adma.202407132.
[11] Partridge IK, Cartie DDR. Delamination resistant laminates by Z-Fiber pinning: Part I manufacture and fracture performance. Compos A Appl Sci Manuf 2005;36(1):55–64. https://doi.org/10.1016/j.compositesa.2004.06.029.
[12] Yudhanto A, Watanabe N, Iwahori Y, Hoshi H. Effect of stitch density on tensile properties and damage mechanisms of stitched carbon/epoxy composites. Compos B Eng 2013;46:151–65. https://doi.org/10.1016/j.compositesb.2012.10.003.
[13] Pingkarawat K, Mouritz AP. Improving the mode I delamination fatigue resistanc of composites using z-pins. Compos Sci Technol 2014;92:70–6. https://doi.org/10.1016/j.compscitech.2013.12.009.
[14] Knopp A, Scharr G. Effect of z-pin surface treatment on delamination and debonding properties of z-pinned composite laminates. J Mater Sci 2014;49(4):1674–83. https://doi.org/10.1007/s10853-013-7851-2.
[15] Francesconi L, Aymerich F. Effect of z-pinning on the impact resistance of composite laminates with different layups. Compos A Appl Sci Manuf 2018;114:136–48. https://doi.org/10.1016/j.compositesa.2018.08.013.
[16] Mouritz AP. Review of z-pinned laminates and sandwich composites. Compos A Appl Sci Manuf 2020;139:106128. https://doi.org/10.1016/j.compositesa.2020.106128.
[17] Yu J, Zhou C, Li S. Experimental and numerical research on the mode I delamination of looped fabric reinforced laminate. Compos B Eng 2020;182:107566. https://doi.org/10.1016/j.compositesb.2019.107566.
[18] Drake DA, Sullivan RW, Lovejoy AE, Clay SB, Jegley DC. Influence of stitching on the out-of-plane behavior of composite materials–a mechanistic review. J Compos Mater 2021;55(23):3307–21. https://doi.org/10.1177/00219983211009290.
[19] Francesconi L, Aymerich F. Damage mechanisms in the CAI failure of thin z-pinned composite laminates. Compos A Appl Sci Manuf 2022;158:106991. https://doi.org/10.1016/j.compositesa.2022.106991.
[20] Chen X, Zheng H, Wei Y, Ren Z. Effect of tufting on the interlaminar bonding behavior of needled composite. Polym Compos 2023;44:229–40. https://doi.org/10.1002/pc.27040.
[21] Loi G, Aymerich F. Effect of stitching on the static and fatigue properties of fibre-dominated and matrix-dominated composite laminates. Compos A Appl Sci Manuf 2023;173:107648. https://doi.org/10.1016/j.compositesa.2023.107648.
[22] Mouritz AP, Cox BN. A mechanistic interpretation of the comparative in-plane mechanical properties of 3D woven, stitched and pinned composites. Compos A Appl Sci Manuf 2010;41(6):709–28. https://doi.org/10.1016/j.compositesa.2010.02.001.
[23] Sarantinos N, Tsantzalis S, Ucsnik S, Kostopoulos V. Review of through-the-thickness reinforced composites in joints. Compos Struct 2019;229:111404. https://doi.org/10.1016/j.compstruct.2019.111404.
[24] Mouritz AP. Review of z-pinned composite laminates. Compos A Appl Sci Manuf 2007;38(12):2383–97. https://doi.org/10.1016/j.compositesa.2007.08.016.
[25] Kostopoulos V, Sarantinos N, Tsantzalis S. Review of through-the-thickness reinforced z-pinned composites. J Compos Sci 2020;4(1):31. https://doi.org/10.3390/jcs4010031.
[26] Chang P, Mouritz AP, Cox BN. Properties and failure mechanisms of pinned composite lap joints in monotonic and cyclic tension. Compos Sci Technol 2006;66:2163–76. https://doi.org/10.1016/j.compscitech.2005.11.039.
[27] Chang P, Mouritz AP, Cox BN. Elevated temperature properties of pinned composite lap joints. J Compos Mater 2008;42(8):741–69. https://doi.org/10.1177/0021998308088594.
[28] Koh TM, Isa MD, Chang P, Mouritz AP. Improving the structural properties and damage tolerance of bonded composite joints using z-pins. J Compos Mater 2012;46(26):3255–65. https://doi.org/10.1177/0021998312437233.
[29] Löbel T, Kolesnikov B, Scheffler S, Stahl A, Hühne C. Enhanced tensile strength of composite joints by using staple-like pins: working principles and experimental validation. Compos Struct 2016;106:453–60. https://doi.org/10.1016/j.compstruct.2013.06.020.

[30] Son HG, Park YB, Kweon JH, Choi JH. Fatigue behaviour of metal pin reinforced composite single-lap joints in a hygrothermal environment. Compos Struct 2014;108:151–60. https://doi.org/10.1016/j.compstruct.2013.09.012.

[31] Ko MG, Kweon JH, Choi JH. Fatigue characteristics of jagged pin-reinforced composite single-lap joints in hygrothermal environments. Compos Struct 2015;119:59–66. https://doi.org/10.1016/j.compstruct.2014.08.025.

[32] Ravindran AR, Ladani RB, Wang CH, Mouritz AP. Design considerations in the strengthening of composite lap joints using metal z-pins. Compos A Appl Sci Manuf 2022;160:107031. https://doi.org/10.1016/j.compositesa.2022.107031.

[33] Dhilipkumar T, Rajesh M. Influence of manufacturing process and GFRP pin loading on shear and dynamic behaviour of composite joints. J Adhes 2023;99(4):538–57. https://doi.org/10.1080/00218464.2022.2025782.

[34] Loi G, Buonadonna P, El Mohtadi R, Carta M, Lai D, El Mehtedi M, et al. Effect of selective Z-pinning on the static and fatigue strength of step joints between composite adherends. J Compos Sci 2024;8(3):84. https://doi.org/10.3390/jcs8030084.

[35] Jin Y, Li Y, Hu Z, Li W, Li L. Study on tensile properties of Z-pin reinforced bismaleimide resin matrix composites with single lap joints. Polym Compos 2025;46:5370–81. https://doi.org/10.1002/pc.29297.

[36] M'membe B, Yasaee M, Hallett SR, Partridge IK. Effective use of metallic Z-pins for composites' through-thickness reinforcement. Compos Sci Technol 2019;175:77–84. https://doi.org/10.1016/j.compscitech.2019.02.024.

[37] Santana de Vega E, Allegri G, Zhang B, Hamerton I, Hallett SR. Improving the delamination bridging performance of Z-pins through the use of a ductile matrix. Compos A Appl Sci Manuf 2022;2022(163):107241. https://doi.org/10.1016/j.compositesa.2022.107241.

[38] Pingkarawat K, Mouritz AP. Comparative study of metal and composite z-pins for delamination fracture and fatigue strengthening of composites. Eng Fract Mech 2016;154:180–90. https://doi.org/10.1016/j.engfracmech.2016.01.003.

[39] Stelzer S, Ucsnik S, Pinter G. Fatigue behaviour of composite–composite joints reinforced with cold metal transfer welded pins. Int J Fatigue 2015;81:37–47. https://doi.org/10.1016/j.ijfatigue.2015.06.004.

[40] Stelzer S, Ucsnik S, Pinter G. Strength and damage tolerance of composite–composite joints with steel and titanium through the thickness reinforcements. Compos A Appl Sci Manuf 2016;88:39–47. https://doi.org/10.1016/j.compositesa.2016.05.020.

[41] Bisagni C, Furfari D, Pacchione M. Experimental investigation of reinforced bonded joints for composite laminates. J Compos Mater 2018;52(4):431–47. https://doi.org/10.1177/0021998317708021.

[42] Benzeggagh ML, Kenane MJCS. Measurement of mixed-mode delamination fracture toughness of unidirectional glass/epoxy composites with mixed-mode bending apparatus. Compos Sci Technol 1996;56(4):439–49. https://doi.org/10.1016/0266-3538(96)00005-X.

[43] Turon A, Camanho PP, Costa J, Renart J. Accurate simulation of delamination growth under mixed-mode loading using cohesive elements: Definition of interlaminar strengths and elastic stiffness. Compos Struct 2010;92(8):1857–64. https://doi.org/10.1016/j.compstruct.2010.01.012.

[44] Schon J. Coefficient of friction of composite delamination surfaces. Wear 2000;237:77–89. https://doi.org/10.1016/S0043-1648(99)00315-4.

[45] ASTM D3039/D3039M-08, Standard Test Method for Tensile Properties of Polymer Matrix Composite Materials, ASTM International West Conshohocken, PA, 2008. Doi:10.1520/D3039_D3039M-08.

[46] ASTM D3518/D3518M-18, Standard Test Method for In-Plane Shear Response of Polymer Matrix Composite Materials by Tensile Test of a $\pm 45^\circ$ Laminate, West Conshohocken, PA, 2018. Doi: 10.1520/D3518_D3518M-18R25.

[47] ASTM D5528/D5528M-13, Standard Test Method for Mode I Interlaminar Fracture Toughness of Unidirectional Fiber-Reinforced Polymer Matrix Composites, ASTM International 2013 West Conshohocken, PA 10.1520/D5528_D5528M-21.

[48] ASTM D7905/D7905M-14, Standard Test Method for Determination of the Mode II Interlaminar Fracture Toughness of Unidirectional Fiber-Reinforced Polymer Matrix Composites, ASTM International 2014 West Conshohocken, PA. Doi: 10.1520/D7905_D7905M-19E01.

[49] Cox BN. Snubbing effects in the pullout of a fibrous rod from a laminate. Mech Adv Mater Struct 2005;12(2):85–98. https://doi.org/10.1080/15376490490493899.